Dipole-coupled core-shell perpendicular-shape-anisotropy magnetic tunnel junction with enhanced write speed and reduced crosstalk

N. Caçoilo, L.D. Buda-Prejbeanu, B. Dieny, O. Fruchart, and I.L. Prejbeanu[*]
Université Grenoble Alpes, CEA, CNRS, Grenoble-INP, SPINTEC, Grenoble 38000, France

The concept of perpendicular-shape-anisotropy spin-transfer-torque magnetic random-access memory tackles the downsize scalability limit of conventional ultrathin magnetic tunnel junctions below sub-20-nm technological nodes. This concept uses a thicker storage layer with a vertical aspect ratio, enhancing the thermal stability factor Δ thanks to the favorable contribution of the shape anisotropy. However, the increased aspect ratio comes with an increase in switching time under applied voltage and the crossover to nonuniform reversal mechanism at higher aspect ratio, limiting the gain in scalability. Additionally, the larger volume of the magnetic cell significantly increases the stray field acting on the neighboring devices compared to thin magnetic tunnel junctions. In this work, we propose the use of a dipole-coupled core-shell system as a storage layer. This improves both bottlenecks, as predicted by micromagnetic simulations for magnetization reversal, and a macrospin model to estimate the stray field in a dense array.

I. INTRODUCTION

Spin-transfer-torque magnetic random-access memory (STT-MRAM) is one of the most promising emerging non-volatile memory technologies. It offers nonvolatility with very large write endurance, high speed, moderate write power, and zero off consumption [1]. The retention time is related to the stability factor Δ of the device, defined as the ratio between the energy barrier (E_B) of the storage layer and the thermal energy ($k_B T$, where k_B is the Boltzmann constant and T is the operating temperature). The energy barrier for the usual perpendicular magnetic tunnel junction (MTJ), made of a stack of ultrathin layers with perpendicular magnetization (p-MTJ), can be expressed as follows, assuming coherent reversal:

$$E_B = AL \left[\frac{k_s}{L} + \frac{1}{2}\mu_0 M_s^2 (N_{xx} - N_{zz}) + K_u \right]. \quad (1)$$

Here A is the device area of the magnetic storage layer, L its height, k_s its surface anisotropy per unit area, μ_0 the vacuum permeability, M_s the spontaneous magnetization, N_{ii} its demagnetizing factors along the plane (xx) and out of the plane (zz), and K_u the bulk uniaxial anisotropy per unit volume. The latter is usually small in conventional p-MTJs, leaving a competition between surface and shape anisotropy.

For a conventional p-MTJ, the lateral dimension of the storage layer is much larger than its height, resulting in a negative and large contribution of the shape anisotropy. This lowers the stability of the out-of-plane state, which is only promoted by surface anisotropy. When the p-MTJ lateral dimension is reduced, the leading variation in Eq. (1) comes through the decrease of A, which decreases the stability. In practice, this limits the scalability of a p-MTJ to diameters of around 20 nm [2].

One proposal to push back this limit is to provide an additional source of total anisotropy energy and thus energy barrier, via the use of a thicker storage layer. Inspecting Eq. (1), we see that this could be achieved in two ways: (1) Decrease, in absolute value, the negative and thus destabilizing impact of the in-plane shape effect per unit volume (the right part, in square brackets), or even make it positive for $L/D > 0.89$ (for a disk shape, with D the cell diameter and thus $A = \pi D^2/4$). (2) Increase the volume prefactor AL, which has a beneficial impact to enhance the energy barrier in the case of perpendicular shape anisotropy (PSA), i.e., for $L/D > 0.89$. This concept has been proven to be effective to extend the range of stability down to sub-10-nm diameter [3,4]. However, this comes at the expense of the need for a larger writing voltage for STT switching, and longer switching time, both being a handicap to applicability.

In this paper, we propose an alternative approach to address the writing drawbacks associated with the thick PSA pillars required at small diameter, introducing a tubular magnetic shell around the storage layer. Making use of the strong dipolar coupling existing in this system thanks

---

[*]Corresponding author: lucian.prejbeanu@cea.fr

to its high vertical aspect ratio, it is possible to promote a core-shell synthetic ferrimagnetic state, with antiparallel storage layer (from now on described as magnetic core) and shell.

The gain introduced by this design is twofold. First, antiparallel coupling enhances stability. This allows a decrease of the total height of the core-shell system to reach a given stability, reducing the volume to switch, and delaying the onset of the domain-wall-based reversal mechanism, thus leading to a lower voltage and faster reversal. Second, the stray field emanating from the composite cell is sharply reduced, enabling a denser array than would be possible for single-pillar PSA-MTJs.

In the following, we first review and refine the evaluation of cell stability (Sec. II). We then present the core-shell concept and the resulting gain in writing (Sec. III). Finally, we describe the additional gain via the reduction of stray field and thus crosstalk (Sec. IV).

II. CAPPING IN SCALABILITY OF A SINGLE PSA STORAGE LAYER

To understand the increased stability quantitatively, it is necessary to calculate the energy barrier of the system with a focus on the magnetostatic energy (related to the shape anisotropy). To calculate this term, we follow the approach used in Refs. [5,6], where a Fourier-space formalism based on the shape amplitude $\mathcal{D}(\mathbf{k})$ (in k-space) of the object is used to compute the demagnetizing factors. For a cylinder, the shape amplitude is given by (in cylindrical coordinates)

$$\mathcal{D}(k_\perp, k_z) = \frac{4\pi R}{k_\perp k_z} \mathcal{J}_1(k_\perp R) \sin\left(\frac{L}{2}k_z\right), \qquad (2)$$

with $k_\perp = \sqrt{k_x^2 + k_y^2}$ relates to the direction perpendicular to the cylinder axis, R is the radius of the magnetic cylinder, and $\mathcal{J}_1(x)$ is the Bessel function of the first kind. It is then possible to calculate the demagnetizing factor along the direction along the axis of the cylinder:

$$\mathcal{N}_{zz} = \frac{1}{8\pi^3 V} \int \frac{d^3\mathbf{k}}{\mathbf{k}^2} |\mathcal{D}(\mathbf{k})|^2 k_z^2. \qquad (3)$$

After a series of integrations and transformations, it is possible to achieve a simpler notation as in Ref. [5],

$$\mathcal{N}_{zz}^{\text{cylinder}} = 1 + \frac{4}{3\pi\tau} - F_0\left(-\frac{1}{\tau^2}\right), \qquad (4)$$

where F_0 is the hypergeometric function, shown here for convenience:

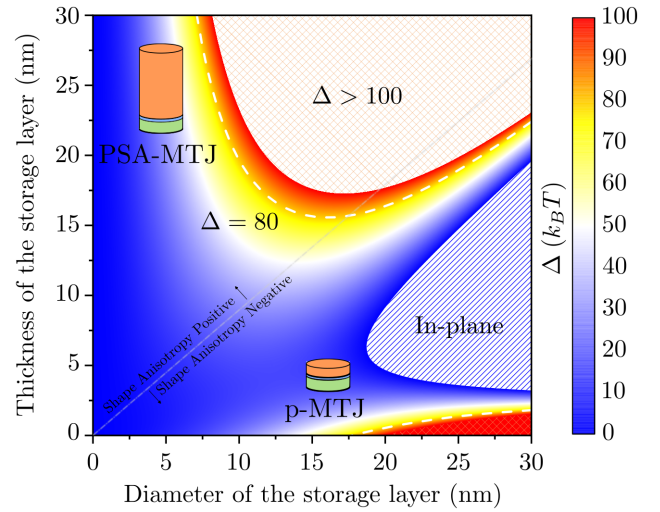$$F_0(x) = {}_2F^1\left(-\frac{1}{2}, \frac{1}{2}, 2, x\right).$$

FIG. 1. Stability factor for different dimensions of the storage layer with a spontaneous magnetization of 1 MA/m for a single MgO interface with a surface anisotropy of 1.4 mJ/m². The pale dashed diagonal line shows the limit between regions with positive and negative values of the magnetostatic energy.

The two identical transverse demagnetizing coefficients can be calculated as $(1 - \mathcal{N}_{zz}^{\text{cylinder}})/2$, and the magnetostatic anisotropy energy coefficient scales with $(1 - 3\mathcal{N}_{zz}^{\text{cylinder}})/2$. Figure 1 shows a stability diagram depending on the geometry of the storage layer (height and diameter) for a storage layer with the usual FeCoB material with spontaneous magnetization of 1 MA/m and a surface anisotropy of 1.4 mJ/m², a typical value in MgO/FeCoB systems. From the diagram, relevant information can be extracted.

Figure 1 illustrates the limitation of the usual p-MTJ at small nodes, as the stability is reduced with the diameter, going below the required levels at around 15 nm diameter (typical for a 10-year retention time, values around $(60\text{–}80)k_BT$ are used). As the height is increased, there is first a reduction in perpendicular stability, as the magnetostatic energy still favors the in-plane orientation, but now its influence is enhanced by the larger volume of the storage layer. This can induce an in-plane alignment of the magnetization, as seen for $D > 18$ nm. However, if the thickness is further increased, there is a stability increase, coming from the progressive reduction of the difference in axis versus transverse demagnetizing factors or even its change in sign, so that perpendicular magnetization is restored as the easy axis. The height necessary to restore perpendicular orientation reduces with reducing diameter (this orientation is aspect-ratio-dependent). Below $D = 18$ nm the easy axis always remains perpendicular. For a cylindrical pillar with a reasonably high surface anisotropy value (as in the example of 1.4 mJ/m²), it is possible to maintain a perpendicular orientation with a large stability down to sub-5-nm diameter. Although at

first glance an effective path for high density, altogether with an exceptional tolerance for high-temperature applications (since the thermal dependence of the magnetization is less steep than that of the surface anisotropy [7–9]), there are still several obstacles that need to be addressed to push this technology forward.

One of the drawbacks of a high-aspect-ratio PSA pillar is to achieve fast and efficient switching with spin-transfer torque, as it is largely an interfacial effect in MTJs [10]. Moreover, there is a capping in stability, due to the formation of a transient domain wall along the height of the storage layer during the magnetization reversal. As already discussed [3], this capping of stability can be determined considering a tail-to-tail domain wall formed along the thickness of the magnetic body, which is dependent on the exchange stiffness A_{ex} and the spontaneous magnetization M_s of the magnetic cylinder:

$$\Delta^{\mathrm{DW}} = \frac{\mu_0 M_s^2}{2 k_B T} \frac{\pi D^2}{4} \left(\frac{D}{2} + L_{\mathrm{DW}} + \frac{2 L_{\mathrm{DW}}^2}{D + 2 L_{\mathrm{DW}}} \right), \quad (5)$$

where L_{DW} is the width of the domain wall, scaling with $\sqrt{4 A_{ex}/(\mu_0 M_s^2)}$.

As the height at which the capping sets in is related to the domain-wall width, a workaround would be to reduce the total height by increasing the surface anisotropy, for example, through an additional MgO interface at the top of the storage layer (as in common double-interface p-MTJs). Experimental efforts have been reported in this direction [11,12]. However, this approach provides moderate gain at lower diameters, as the contribution of the surface anisotropy is less significant. This is observed in Fig. 2, where the stability capping is shown for different thick layers (Co, FeCoB, and Py), with double FeCoB interfaces, with different surface anisotropies of 1.4 and 1.0 mJ/m^2. On this graph, we also see that, the lower the magnetization, the larger the height needs to be to achieve a given stability, as for these diameters the main anisotropy source is magnetostatic.

III. CORE-SHELL CONCEPT FOR THE STORAGE LAYER

To understand the increase in scalability provided by the magnetic shell, it is helpful to first calculate its stability as an isolated element. Thus, we need to calculate its demagnetizing factors, since the shape anisotropy is the only source of magnetic anisotropy. To do so, we use the shape amplitude of Eq. (2), with outer radius R_2 and inner radius R_1 [13,14]:

$$\mathcal{D}(k_\perp, k_z) = \frac{4\pi}{k_\perp k_z} [R_2 \mathcal{J}_1(k_\perp R_2) \\ - R_1 \mathcal{J}_1(k_\perp R_1)] \sin\left(\tfrac{1}{2} L k_z\right). \quad (6)$$
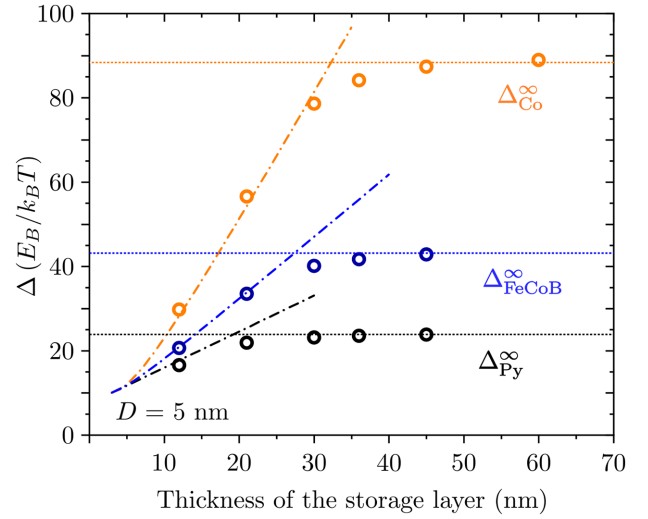

FIG. 2. Stability factor for different PSA storage layers for a 5-nm-diameter storage layer with FeCoB double interface (1.4 and 1.0 mJ/m^2). Predictions based on macrospin are shown with dashed-dotted lines, while the capping of stability related to domain-wall nucleation-propagation is shown with horizontal dotted lines. The open circles stand for micromagnetic simulations of the minimum-energy path.

Following the same reasoning as before, and performing the transformations $q = k_\perp R_2$, $\sigma = R_1/R_2$, and $\tau = L/(2 R_2)$, we obtain the integral

$$\mathcal{N}_{zz}^{\mathrm{shell}}(\sigma, \tau) = \frac{1}{\tau(1 - \sigma^2)} \\ \times \int_0^{+\infty} \frac{\mathrm{d}q}{q^2} (1 - e^{-2q\tau}) [\mathcal{J}_1(q) - \sigma \mathcal{J}_1(\sigma q)]^2. \quad (7)$$

The latter can be expanded to be written with the demagnetizing coefficients of full cylinders ($\sigma = 0$):

$$\mathcal{N}_{zz}^{\mathrm{shell}}(\sigma, \tau) = \frac{1}{1 - \sigma^2} \left[\mathcal{N}_{zz}^{\mathrm{cylinder}}(\tau) + \sigma^2 \mathcal{N}_{zz}^{\mathrm{cylinder}}\left(\frac{\tau}{\sigma}\right) \\ - \frac{\sigma^2}{\tau} F_0(\sigma^2) + \frac{2\sigma}{\tau} A_{1,1}^{-1}(2\tau, 1, \sigma) \right], \quad (8)$$

with

$$A_{1,1}^{-1}(2\tau, 1, \sigma) = \int_0^{+\infty} q^{-2} e^{2q\tau} \mathcal{J}_1(q) \mathcal{J}_1(\sigma q) \, \mathrm{d}q, \quad (9)$$

which can be solved by making use of a combination of elliptical integrals (see, for reference, Eq. (10) and Table 1 of Ref. [14]).

Using Eq. (8) it is possible to calculate the preferred orientation of the magnetization in the magnetic shell, as a function of the aspect ratio τ and σ. Figure 3 illustrates
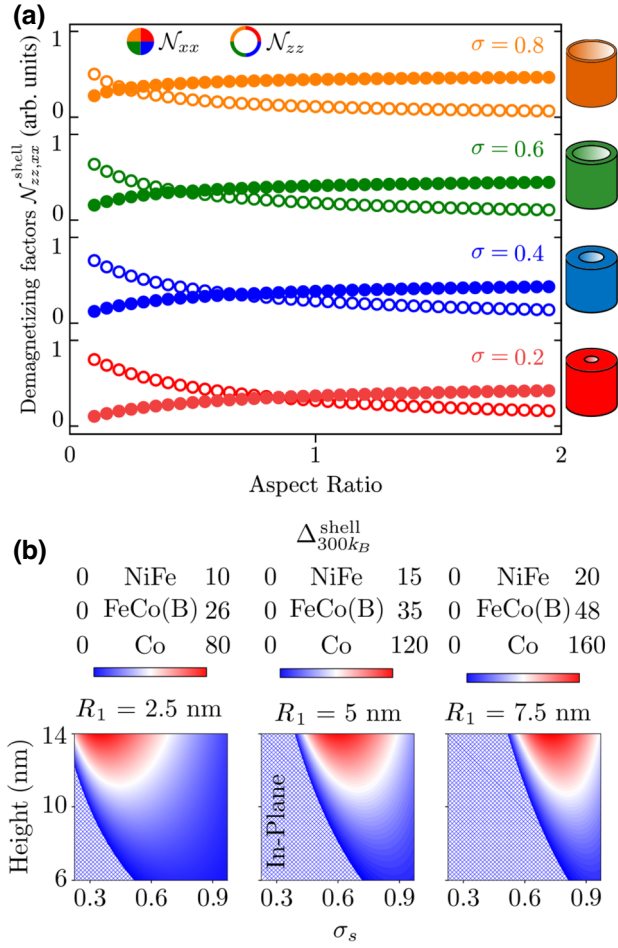
FIG. 3. (a) Demagnetizing factors $\mathcal{N}_{xx}$ (filled circles) and $\mathcal{N}_{zz}$ (open circles) for the magnetic shell as a function of the aspect ratio $\tau = L/(2R_2)$ for different values of σ. (b) Stability factor of the shell as a function of the shell thickness ratio σ and aspect ratio τ^{shell} for three different inner radius R_1 values for the situation of a Ni shell 0.489 MA/m, NiFe shell 0.756 MA/m, and Co shell 1.446 MA/m. The patterned region shows the in-plane orientation of the magnetization.

this versus aspect ratio, for several values of σ. There are two important features to be extracted: The crossing point between the $\mathcal{N}_{xx}^{\text{shell}}$ and $\mathcal{N}_{zz}^{\text{shell}}$ curves highlights the crossover between the in-plane versus perpendicular easy directions. This occurs at smaller aspect ratios as the value of σ gets larger, as the shell resembles a thin rolled sheet. In the opposite situation of small σ, the aspect ratio for crossover is similar to that of a full cylinder. Above the crossover, the difference between the two demagnetizing factors keeps increasing as the aspect ratio increases, which is likely to provide a larger stability to the magnetic shell.

This stability, the product of the volume of the shell and the difference of its demagnetizing coefficients shown in Fig. 3(a), is displayed in Fig. 3(b) versus the height of the shell and σ (R_1/R_2), for different radii of the inner shell

(columns) and different materials (rows). Consistent with Fig. 3(a), perpendicular anisotropy is promoted by a high aspect ratio and small shell thickness ($R_2 - R_1$). In these diagrams, we clearly see that, in the case of perpendicular anisotropy, the regions with highest stability are those for rather thick shells (low σ), which comes from its large volume and therefore a large energy barrier. Also, as is the case with standard PSA pillars, the stability scales with M_s^2.

We now turn to considering both the core and the shell in dipolar interaction to evaluate how the various geometrical parameters can be best tuned to enhance stability. In addition to R_1, R_2, and L already described, we introduce R_0 as the radius of the core cylinder, with $R_0 < R_1 < R_2$.

As described in Ref. [14], the dipolar coupling energy of the core and the shell (E_{cs}) is given by the interaction between the shape amplitudes of the two objects:

$$E_{cs} = \frac{\mu_0 M_{\text{core}} M_{\text{shell}}}{8\pi^3}$$
$$\times \int \frac{d\mathbf{k}}{k^2} D_{\text{core}}(\mathbf{k}) D_{\text{shell}}(\mathbf{k}) (\mathbf{m}_1 \cdot \mathbf{k})(\mathbf{m}_2 \cdot \mathbf{k}), \quad (10)$$

where D_{core} and D_{shell} are defined by Eqs. (2) and (6), respectively. Equation (10) can be formally simplified to

$$E_{cs} = \pi \mu_0 M_{\text{core}} M_{\text{shell}} R_0$$
$$\times [2\cos\theta_1 \cos\theta_2 - \sin\theta_1 \sin\theta_2 \cos(\phi_1 - \phi_2)]$$
$$\times \int_0^{+\infty} \frac{dk_\perp}{k_\perp^2} [R_2 \mathcal{J}_1(k_\perp R_2) \mathcal{J}_1(k_\perp R_0)$$
$$- R_1 \mathcal{J}_1(k_\perp R_1) \mathcal{J}_1(k_\perp R_0)](1 - e^{-k_\perp L}). \quad (11)$$

Compared with the initial approach [14,15], we expand the modeling to the case in which the shell is not in contact with the magnetic shell. Making use of $q_i = k_\perp R_i$, $\sigma_i = R_0/R_i$, and $\tau_i = L/(2R_i)$ (where i is related to the inner radius R_1 and outer radius R_2), the integral of Eq. (11) can be further expanded to

$$\mathcal{J}_{cs} = \frac{1}{R_0^2} \int_0^{+\infty} \frac{dq_2}{\sigma_2^2 q_2^2} \mathcal{J}(q_2)\mathcal{J}(\sigma_2 q_2)(1 - e^{-2q_2\tau_2})$$
$$- \int_0^{+\infty} \frac{dq_1}{\sigma_1^2 q_1^2} \mathcal{J}(q_1)\mathcal{J}(\sigma_1 q_1)(1 - e^{-2q_1\tau_1}). \quad (12)$$

Making use of the last results from Eqs. (8) and (9), it is possible to get the results for the dipolar coupling of the core and shell $\mathcal{J}_{cs}$ as

$$\mathcal{J}_{cs} R_0^2 = \frac{1}{\sigma_2^2}[\sigma_2 F_0(\sigma_2^2) + A_{1,1}^{-1}(2\tau_2, 1, \sigma_2)]$$
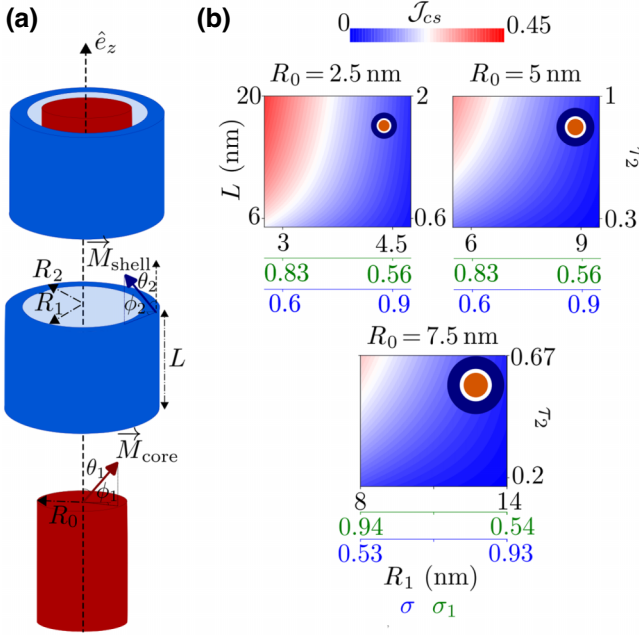$$- \frac{1}{\sigma_1^2}[\sigma_1 F_0(\sigma_1^2) + A_{1,1}^{-1}(2\tau_1, 1, \sigma_1)]. \quad (13)$$

FIG. 4. (a) Schematics of the core-shell system, where R_0 is the inner radius of the magnetic core (red) with magnetization orientation $\vec{M}_{\text{core}}$ with angles θ_1, ϕ_1, and magnetic shell (blue) with magnetization orientation $\vec{M}_{\text{shell}}$ with angles θ_2, ϕ_2. Both parts have a common thickness of L. (b) Dipolar coupling magnitude $\mathcal{J}_{cs}$ for a fixed value of $\sigma_2 = 0.5$ for different R_0, as a function of the thickness L and inner radius R_1.

In addition, these results can be linked to the demagnetizing factors of the shell and core through Eq. (8).

In the end, the dipolar coupling energy depends on the geometry, and it is proportional to the magnetization of both the shell and the core:

$$E_{cs} = \mu_0 \pi R_0^3 M_{\text{core}} M_{\text{shell}} \times \underbrace{\mathcal{J}_{cs}(\tau_0, \tau_1, \tau_2, \sigma_1, \sigma_2)}_{\text{geometrical scaling factor}}$$

$$\times (2\cos\theta_1 \cos\theta_2 - \sin\theta_1 \sin\theta_2). \quad (14)$$

The dependence of the scaling factor ($\mathcal{J}_{cs}$) versus the system's geometry is illustrated in Fig. 4 for different values of the core radius R_0 and keeping constant the ratio $\sigma_2 = 0.5$. Thus, the three plots differ in core radius, the separation between the inner shell and core, as well as the ratio between the inner and outer radii of the shell $\sigma_s = R_1/R_2$. It can be seen that a stronger geometrical scaling is achieved at thinner separations and larger aspect ratios. Besides tuning $\mathcal{J}_{cs}$, the total dipolar coupling energy can be further increased through an increase in R_0, related to the magnetic volume, or through the increase in the magnetization of both the shell and the magnetic core $M_{\text{core}} M_{\text{shell}}$.

TABLE I. Coefficients of the energy of the coupled core-shell systems shown on Fig. 5 in units of $k_B T$, i.e., for different heights and fixed core-shell radius of $R_0 = 7$ nm, $R_1 = 8$ nm, and $R_2 = 10$ nm.

Height (nm)	$\mathcal{A}$ ($k_B T$)	$\mathcal{B}$ ($k_B T$)	$\mathcal{C}$ ($k_B T$)
6	15	17	19
8	22	43	25
10	30	72	32
12	42	100	35

As a final step, we now compute the total energy of the dipole-coupled core-shell magnetic system, E_{tot}, as [14]

$$E_{\text{tot}}(\theta_1, \theta_2, \phi_1, \phi_2)$$
$$= E_c \sin^2\theta_1 + E_s \sin^2\theta_2 + E_{cs}(\theta_1, \theta_2, \phi_1, \phi_2), \quad (15)$$

where E_c is the energy barrier of the isolated magnetic core, E_s is that of the shell alone, and E_{cs} is the coupling energy. For the sake of simplicity and generality, we write the energy of the system using the coefficients $\mathcal{A}, \mathcal{B}, \mathcal{C}$, and $\mathcal{D}$ for the different angular dependences:

$$E_{\text{tot}} = \mathcal{A}\sin^2\theta_1 + \mathcal{B}\sin^2\theta_2$$
$$- \mathcal{C}\sin\theta_1 \sin\theta_2 \cos(\phi_1 - \phi_2) + \mathcal{D}\cos\theta_1 \cos\theta_2. \quad (16)$$

In the above equation, $\mathcal{A}$ is the self-energy barrier of the magnetic core, $\mathcal{B}$ the self-energy barrier of the magnetic shell, and $\mathcal{C}$ and $\mathcal{D}$ are the core-shell coupling energies in the parallel state for the transverse and axial directions, respectively. With the present geometry, all four coefficients are positive and $\mathcal{D} = 2\mathcal{C}$; see Eq. (11). Thus, the lowest-energy state is expected when both shell and core are out-of-plane magnetized and antiparallel to one another, and the most energetic state occurs when both shell and core are in-plane magnetized and antiparallel to one another. More generally, for arbitrary θ_1 and θ_2, inspection of Eq. (15) shows that the minimum-energy path for switching is expected to satisfy $\phi_1 = \phi_2 + \pi$ at all times, which we consider satisfied from now on.

The angular dependence of the energy barrier described by Eq. (16) is shown in Fig. 5(a), for the case of a fixed core radius of 7 nm, a shell inner radius of 8 nm, and an outer radius of 10 nm for several lengths (6, 8, 10, and 12 nm). The core magnetization is 1 MA/m, the surface anisotropy is 1.4 mJ/m^2, and the shell magnetization is 1.446 MA/m. The corresponding coefficients $\mathcal{A}$, $\mathcal{B}$, and $\mathcal{C}$ involved in the dipolar energy are listed in Table I. For each vertical aspect ratio, the minimum-energy path is computed [16] and displayed in Fig. 5(b).

In all four cases, we confirm that the ground state is perpendicular anisotropy in an antiparallel state. The energy barrier increases with the vertical aspect ratio, as expected
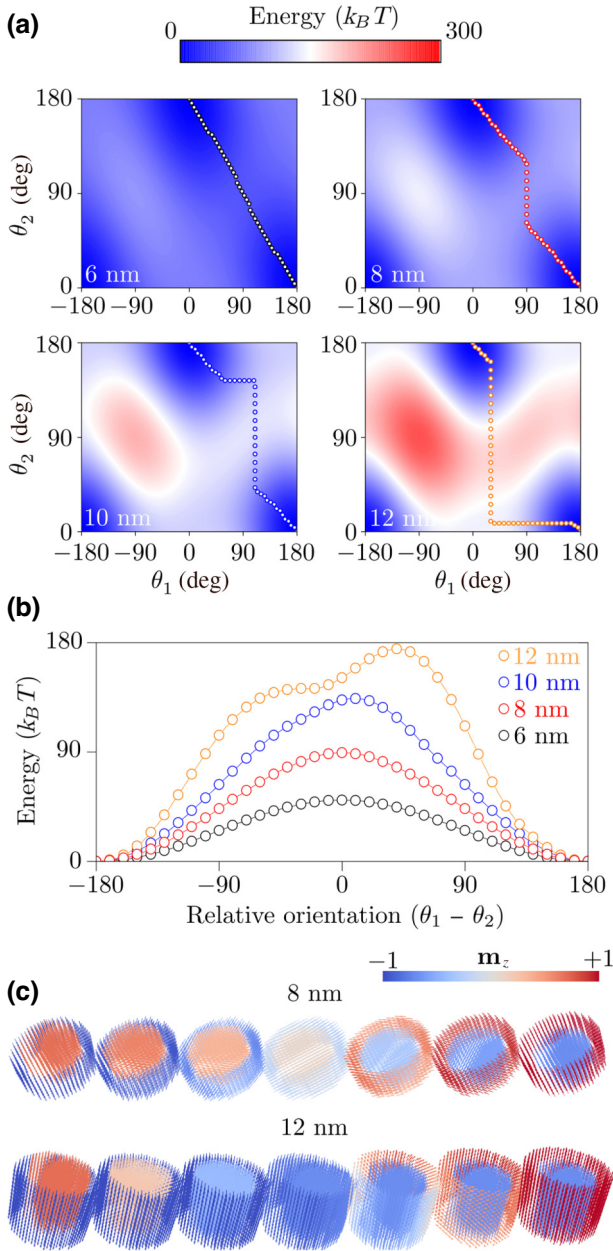
(a)

(b)

(c)

FIG. 5. (a) Angular dependence of the energy barrier of the magnetic system for different core-shell lengths with a fixed core radius of 7 nm, inner shell radius of 8 nm, and outer radius of 10 nm, for the saturation magnetization of 1 MA/m for the magnetic core and 1.446 MA/m for the magnetic shell. Negative angles can be viewed as standing for the case $\phi_1 = \phi_2 + \pi$, while formally only positive angles are defined in spherical coordinates. The trace of the minimum-energy path for each geometry is shown with the small circles. (b) Relative orientation of the minimum-energy path for increasing thickness of the core-shell system. (c) Three-dimensional snapshots for the heights of 8 and 12 nm, along the minimum-energy path.

from our previous discussion on individual core, individual shell, and dipolar coupling. For the system with height 6 nm, the minimum-energy path is a line with slope -1,

which means that the two parts rotate simultaneously. We indeed expect this if the coupling between shell and core is comparable or even larger than the anisotropy energy of each element taken separately, which is the case here. To the contrary, in the system with height 12 nm the coupling is smaller than any of the energy barriers of the two elements taken independently. This implies that a sequential reversal allows the total energy barrier to be minimized, which indeed is seen in the energy maps and the energy plot in Fig. 5(b). The heights 8 and 10 nm appear as crossover situations, with a combination of sequential and coupled paths.

From a device point of view, a strong coupling situation may imply a prohibitively large energy barrier, while the weak coupling one is not suited either if only the core is connected through the leads for STT switching, as the coupling is not sufficient to switch the shell once the core has been switched. Thus, we expect that the optimum situation is to be found in the crossover regime, to be identified using simulation.

The discussion of the energetics of a coupled set of macrospins and its minimum-energy path is valuable to draw the general trends and identify the suitable range of operating parameters. Now, we turn to micromagnetic simulations to refine the conclusions and determine the optimal geometrical and magnetic parameters in the framework of the PSA-MTJ, taking into account precessional effects, the excitation means (current injected via an MTJ in the core only), and possible nonmacrospin effects. For this purpose, we use a finite-difference three-dimensional (3D) micromagnetic solver with a cubic computational cell of 1 nm^3 [10,17], in which the magnetization dynamics is described by the Landau-Lifshitz-Gilbert-Slonzcewski (LLGS) equation.

Here we consider that an injected spin-polarized current interacts with the magnetic body of the core via a damping-like torque (Γ_{STT}), while we neglect the effect of the field-like torque:

$$\partial_t \mathbf{m} = -|\gamma| \mu_0 (\mathbf{m} \times \mathbf{H}_{\text{eff}}) + \alpha (\mathbf{m} \times \partial_t \mathbf{m}) + \Gamma_{\text{STT}}, \quad (17)$$

with γ the gyromagnetic ratio, and

$$\Gamma_{\text{STT}} = -|\gamma| a_{\parallel} V \mathbf{m} \times (\mathbf{m} \times \mathbf{m}_{\text{RL}}), \quad (18)$$

where V is the applied bias voltage, $\mathbf{m}$ is the unit vector for magnetization of the storage layer at the location considered, $\mathbf{m}_{\text{RL}}$ is the unit vector for magnetization of the reference layer, and $a_{\parallel}$ is the STT prefactor. The latter is expected to physically decay along the thickness of the magnetic body through the interaction with magnetization [18,19].

Contrary to the case of ultrathin MTJs, the torque is expected to be largely nonhomogeneous and predominantly exerted close to the interface with the tunnel barrier.

To reflect this, we apply the full STT torque in the first layer of cells, whose strength matches the expected torque integrated when moving away from the interface, with an exponential decay

$$\langle a_\parallel \rangle = a_\parallel(0) \times \sum_{n=0}^{N-1} \exp\left(\frac{-n\lambda_{\mathrm{STT}}}{\delta_z}\right), \qquad (19)$$

in which λ_{STT} is the characteristic STT decay length (taken as 1 nm) and δ_z is the cell size (1 nm). Making use of the definition

$$a_\parallel(0) = \frac{\hbar}{2e} \frac{\eta_{\mathrm{STT}}}{R \times A} \frac{1}{M_s \delta_z}, \qquad (20)$$

where η_{STT} is the STT efficiency [20], it is possible to calculate the strength of the equivalent interfacial STT prefactor. In this study, we consider that the core and thus the interface with MgO is made of a FeCoB base alloy, with spontaneous magnetization of $M_s = 1$ MA/m, exchange stiffness of $A_{\mathrm{ex}} = 15$ pJ/m, and a damping value of $\alpha = 0.01$, $a_\parallel = 140$ mT/V considering a typical tunnel magnetoresistance value of 100% and a $R \times A$ product of 1.5 $\Omega\,\mu m^2$. The voltage is only applied at the interface of the magnetic core, so that the dynamics of the magnetic shell may result only from its dipolar interaction with the core. Surface anisotropy is considered to be present only at the interface between the core and the tunnel barrier, with a value of 1.4 mJ/m^2.

We considered the switching dynamics for two different material parameters for the magnetic shell. The first situation makes use of the system presented in Fig. 5 with a length of 8 nm (chosen such that the stability determined from the minimum-energy path is around 80 $k_B T$), $R_0 = 7$ nm, $R_1 = 8$ nm, and $R_2 = 10$ nm, where a magnetic shell of Co is used, with M_s of 1.446 MA/m, exchange stiffness A_{ex} of 15 pJ/m, and damping either $\alpha = 0.01$ or $\alpha = 0.1$. The applied voltage is -1 V.

The time trace of the mean perpendicular magnetization components of the core, shell, and full system are shown in Fig. 6. The magnetization switching of the isolated magnetic core (without magnetic shell) happens at an earlier stage compared with the core coupled with a magnetic shell. This is expected, since the core alone has a lower stability, around 22 $k_B T$, and it is also not stabilized along the initial direction by the stray field of the shell. When considering the shell, we can see that its reversal is delayed with respect to that of the core, which makes sense, as current is injected only into the latter. Besides, the switching of the core is delayed in the case of a shell with higher damping, which we attribute to an incubation effect, with a lower efficiency to set in precessional dynamics: part of the injected energy may be absorbed in the shell, via dipolar coupling. A striking effect is that, for lower damping of the shell, even though both the core and the shell start their
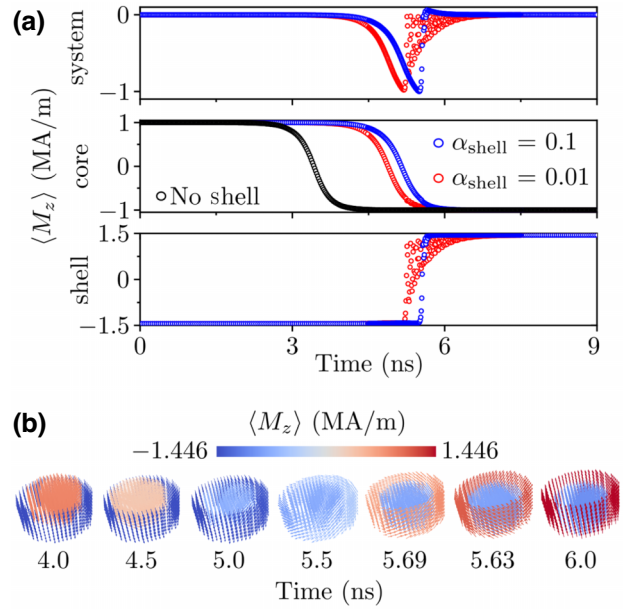

FIG. 6. (a) Time trace of the mean magnetization components $\langle M_z \rangle$ for a core-shell system, considering two different damping parameters for a Co magnetic shell. The top plot shows magnetization averaged over the entire composite system, while the bottom plots show the components of the core and shell independently. (b) 3D snapshots of the time evolution of a core-shell system under an applied voltage of -1 V for the situation of low and high damping. The color bar shows the magnitude of the z component of the average magnetization in each computational cell.

reversal faster, the shell takes longer to relax to the stable final state. Indeed, if the damping of the shell is large, then the incubation time for precession is longer, but then there is a faster relaxation to the stable state. This is consistent with the large oscillations of perpendicular magnetization seen in the case of lower damping.

We now consider a shell made of a low-magnetization material, considering Ni with spontaneous magnetization of 489 kA/m and exchange stiffness of 8 pJ/m, again for both low- and high-damping situations (Fig. 7). As concerns the switching time of the core, it is seen that it is similar to that without a magnetic shell, both in incubation time and switching dynamics, and it is also barely dependent on the damping parameter of the shell. This is understandable, as the lower stray field of the shell has a lower stabilizing effect than that shown on Fig. 6; and also it will be less effective in pumping energy out of the initial oscillations during the incubation time.

As concerns the shell, a close examination of the time scale shows that its reversal starts when the core has not fully reversed, but rather has an in-plane magnetization. Besides, its reversal takes longer than for a high-magnetization shell (Fig. 6), especially for low damping. This may result from the small energy barrier of the

(a)

(b)
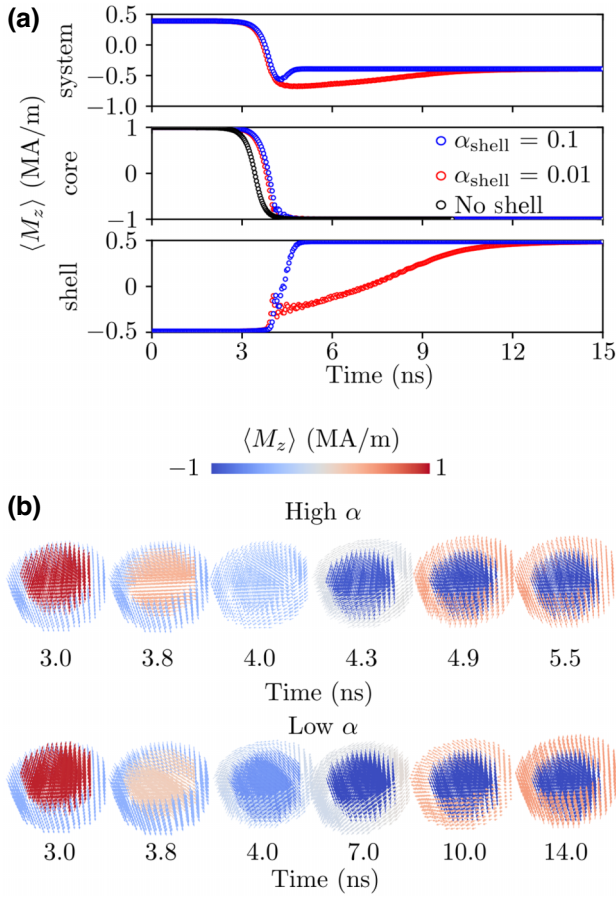
High α

Low α

FIG. 7. (a) Time trace of the mean magnetization components $\langle M_z \rangle$ for a core-shell system, considering two different damping parameters for a Ni magnetic shell. The top plot shows magnetization averaged over the entire composite system, while the bottom plots show the components of the core and shell independently. (b) 3D snapshots of the time evolution of a core-shell system under an applied voltage of -1 V for the situation of low and high damping. The color bar shows the magnitude of the z component of the average magnetization in each computational cell.

magnetic shell (around 5 $k_B T$), so that it is mostly and directly affected by the dipolar coupling with the magnetic core. Figure 7(b) shows 3D snapshots of the reversal for the high- and low-damping situations, illustrating the ringing effect in the latter.

It is relevant to compare the speed of this somewhat complex reversal with that of the usual PSA-MTJ. Figure 8 shows a comparison between the switching time (time required for the magnetization to lie in-plane) of a 20-nm PSA-MTJ with similar Δ to the core-shell structure shown in Fig. 6. For the situation of larger shell damping ($\alpha = 0.1$), one can observe a faster reversal for the magnetic core (already observed is an almost instant reversal of both shell and core), at similar switching voltages to that of the PSA-MTJ. This is striking in several ways. Firstly, we expect
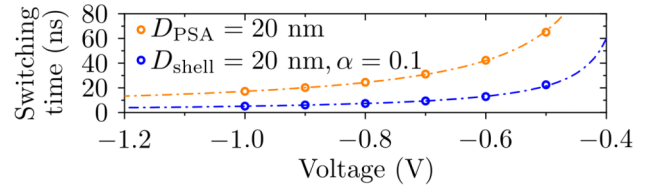

FIG. 8. Dependence of the switching time as a function of the applied voltage for a usual PSA-MTJ cell with 20 nm diameter and a height of 16.5 nm (orange) and for a core-shell cell (properties of Fig. 6) with a shell damping of $\alpha = 0.1$ (blue).

larger switching voltages at lower diameters [10], which is not the case, showing that the core-shell system can compete with a larger-diameter PSA-MTJ. Additionally, the switching time is faster for the core-shell system, although both Δ values are similar. This is largely attributed to a thinner height, with associated larger STT effect.

In conclusion, all geometrical and magnetic parameters influence the switching process in a core-shell process. Namely, the effect of a truncated shape for the PSA-MTJ (and consequently the core-shell PSA-MTJ) brought about by the fabrication process will most likely impact the switching time and stability. Unlike the case of simple MRAM cells, either flat or PSA, higher damping may be beneficial in the shell. In practice, the parameter space should probably be explored in more detail to meet the desirable criteria of any given situation, in terms of stability, switching time, and power consumption.

IV. REDUCED CROSSTALK MAKING USE OF THE CORE-SHELL CONCEPT

We examine here another advantage of the core-shell storage layer, which is the possibility to mitigate the mutual coupling via the stray field from neighboring bits in a highly dense array via the optimization of both geometry and magnetic properties. To evaluate the gain quantitatively, we compute the magnetic field emanating from a pillar with the formalism implemented in Ref. [21].

Starting from the magnetic potential, it is possible to derive the radial (H_r) and perpendicular (H_z) components of the magnetic field, respectively:

$$H_r(r,z) = 2\pi R_0 M_s \int_0^\infty dk \, [e^{-k|Z-L|} - e^{-k|Z|}]$$
$$\times \mathcal{J}_1(kr)\mathcal{J}_1(kR_0), \qquad (21)$$

$$H_z(r,z) = 2\pi R_0 M_s \int_0^\infty dk \, [\mathrm{sign}(Z-L)e^{-k|Z-L|}$$
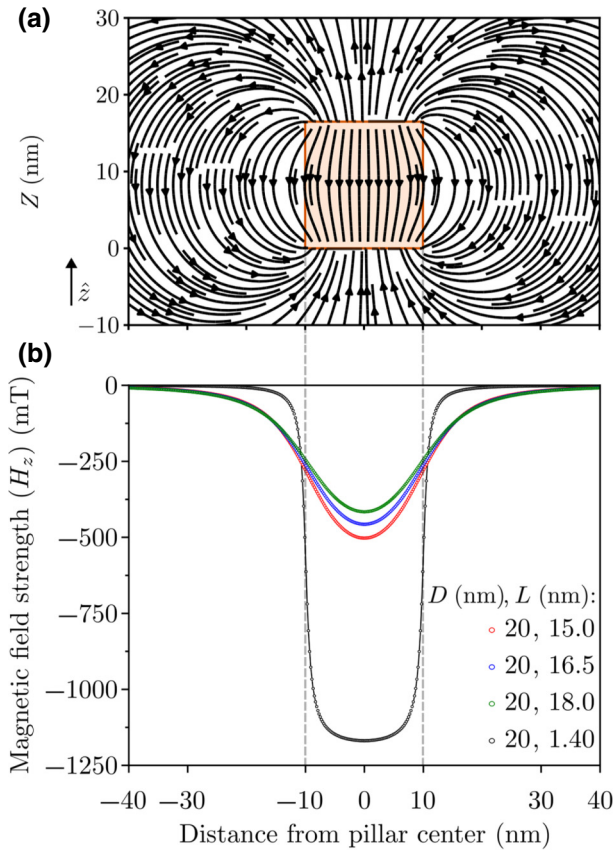$$- \mathrm{sign}(Z)e^{-k|Z|}]\mathcal{J}_0(kr)\mathcal{J}_1(kR_0), \qquad (22)$$

FIG. 9. (a) Two-dimensional (2D) stray-field lines arising from a pillar with high aspect ratio (thickness of 16.5 nm and 20 nm diameter; orange region) with up magnetization along $\hat{z}$. (b) Magnetic field strength at mid-thickness of the magnetic pillar, for four different aspect ratios.

FIG. 10. Volume-averaged stray field at the central pillar in a 5×5 array for (a) PSA-MTJs with a diameter of 20 nm and height 16.5 nm and (b) p-MTJs with a diameter of 20 nm and thickness 1.4 nm. The contribution from the first shell of neighbors is shown with black open circles. The contribution of the second shell of neighbors is shown with red open circles. The sum of both contributions is shown with blue open circles. The dependence of the thermal stability as a function of the pitch for both PSA-MTJ and p-MTJ is shown as an inset in panel (b).

where $\mathcal{J}_x$ are Bessel functions of order x, R_0 is the radius of the magnetic cylinder, L is its height, and M_s is its spontaneous magnetization. These equations can be used to calculate both the demagnetizing field (inside the magnetic body $0 < Z < L$ and $r < R_0$, since there is a discontinuity for $Z = L$ and $Z = 0$ and $r < |R_0|$) and the stray field outside (for $Z > L$ and $r > |R_0|$).

These are displayed in Fig. 9(a) for a magnetic pillar with $2R_0 = 20$ nm diameter and height $L = 16.5$ nm. We consider perpendicular magnetization, which in practice would arise from the combination of shape and surface anisotropy. The magnetic field strength at mid-height of the pillar is shown in Fig. 9(b) for pillars with different aspect ratios, all assumed to have perpendicular magnetization. In the situation of a low aspect ratio (such as the usual p-MTJ with 20 nm diameter and 1.4 nm height), we can observe a thin-film-like demagnetizing field for $r < |R_0|$, with a sharp decay outside the pillar. For PSA-like pillars, the demagnetizing field is reduced, but the stray field is greatly enhanced due to the larger volume involved and hence the magnetic moment. As in two dimensions, the
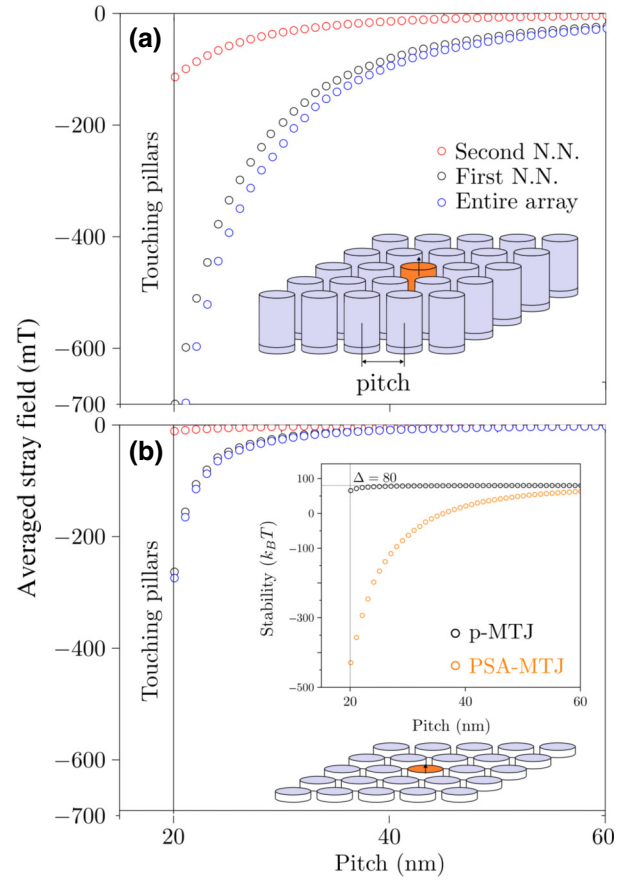
extension of the stray field is short-ranged, typically of the order of the system thickness or so [22]. One may evaluate its impact based on a finite and small array, which we do in the following.

To evaluate the strength of the stray field in a dense array of pillars with perpendicular magnetization, we consider a 5×5 pillar array, as depicted in Fig. 10. We define the pitch as the distance between the centers of two adjacent pillars, and thus, when in contact, it equals the pillar diameter. We do not consider the stray field arising from a possible reference layer below the pillar, as this can be engineered to be negligible [23].

Figure 10 shows the stray field in an array as a function of its pitch, for pillars of high vertical aspect ratio [20 nm diameter and 16.5 nm height, Fig. 10(a)], and for cells with a flat aspect ratio [20 nm diameter and 1.4 nm height, Fig. 10(b)], both with spontaneous magnetization
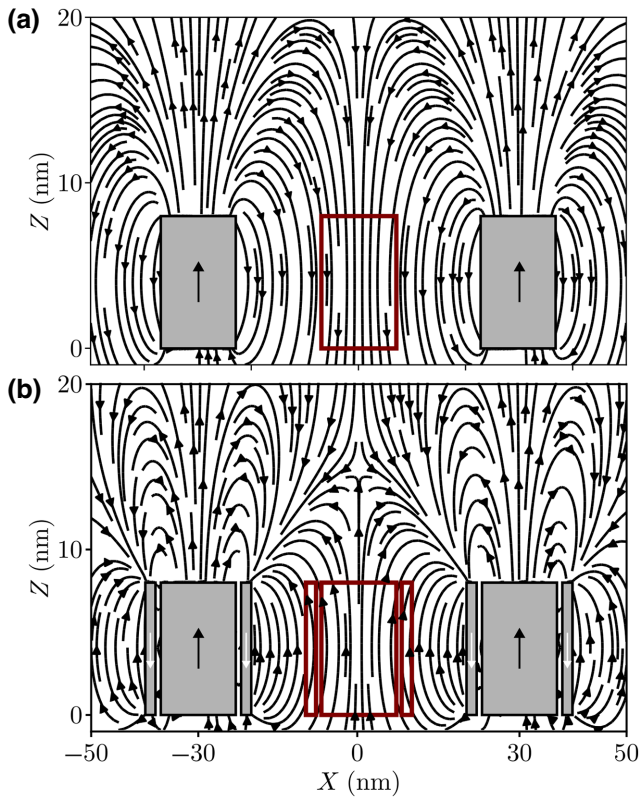
FIG. 11. 2D stray-field lines of (a) two magnetic cores with a pitch of 30 nm. Each magnetic core has a diameter of 14 nm and a height of 8 nm and of (b) two core-shell systems with a pitch of 30 nm. Each system is composed of a magnetic core with a radius of 7 nm, inner shell radius 8 nm, an outer shell radius 10 nm, and a height of 8 nm. In both situations, the system is shown with a filled gray color, and the magnetization direction of the core is shown in black, pointing up. For the core-shell situation, the magnetization of the shell is white, pointing down. In both cases, the central element is shown in an orange-red colour.

of 1 MA/m. These situations correspond, respectively, to PSA-MTJs and p-MTJs. Both panels show the contribution of the first shell, the second shell, and the total. For p-MTJs, the stray field is significant when pillars are in contact, but becomes negligible for pitch 50 nm or greater, as is standard for usual integration processes [24]. The impact of the second shell of neighbors is insignificant in all cases, so considering the impact of the first nearest neighbors is enough [25]. For PSA-MTJs, the stray field from the first shell is stronger, and that of the second is non-negligible. The next shells may be safely ignored thanks to the $1/r^2$ decay of the stray field emanating from a complete shell.

The resulting total stray field is very significant and is expected to affect the stability factor of the device ($\Delta^0 \setminus k_B T$). This can be increased (reduced) if the average stray field points in the same (opposite) direction as the pillar
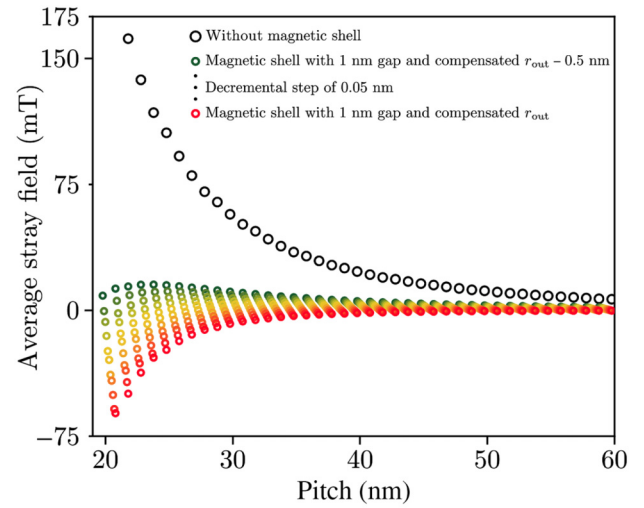

FIG. 12. Volume-averaged stray field at the central pillar in an array of PSA-MTJs with a diameter of 20 nm and height 16.5 nm as a function of the pitch for the situations of unshelled pillar (black open circles) and shelled pillars (colored open circles) for an inner radius of 8 nm and different outer radius, from compensated magnetic volume (red open circles) to a 0.5 nm smaller outer radius.

magnetization [26]:

$$\Delta_{k_B T}^{\mathrm{stray}} = \Delta^0 \setminus k_B T \left(1 \pm \frac{H_z^{\mathrm{stray}}}{H_K^{\mathrm{eff}}} \right), \qquad (23)$$

where H_K^{eff} is the effective anisotropy field of the magnetic element and H_z^{stray} is the average stray field felt by it. Both increase and decrease of stability are detrimental for device operation, the former related to the write operation, the latter related to the thermal stability [25]. The dependence of the stability on the pitch of the array is shown in the inset of Fig. 10(b). In the case of an array of p-MTJs, it is seen that a pitch around 30 nm is sufficient to avoid a significant variation in stability. This is related to the fact that in 2D systems the range of dipolar interactions scales with the height of the system. To the contrary, for PSA-MTJ, it would be necessary to drastically increase the pitch to 100 nm or more to reach the same level of crosstalk reduction. The stray field would even be enough to flip the magnetization of the central pillar smaller than 50 nm.

We expect that the core-shell design can also contribute to a mitigation of the stray field from the neighboring dots, thanks to the antiparallel and mostly compensated core and shell magnetic moments. This is illustrated in Fig. 11, considering the effect of two neighboring cells with center-to-center distance of 30 nm, each with a CoFeB core with 14 nm diameter and 8 nm height. Figure 11(a) shows the case of a simple pillar, while in Fig. 11(b) these are surrounded by a shell of Co with an inner shell radius of

8 nm, an outer shell radius of 10 nm. The field lines are indeed drastically different in the core-shell system, characteristic of a quadrupolar arrangement, as the core and shell moments are nearly balanced, in contrast with the situation with no magnetic shell, characteristic of a dipolar system.

Figure 12 quantitatively shows the volume-averaged dipolar field felt by the core of the central cell in a 5×5 array, for the case of a core radius of 7 nm with spontaneous magnetization of 1 MA/m, an inner shell radius of 8 nm, and a varying outer shell radius from the situation where there is compensation of magnetic volume ($M_c V_c = M_s V_s$, where V_c or V_s is the volume from the core or shell) down to smaller outer radius, with a spontaneous magnetization of 1.446 MA/m. Small variations in the outer radius lead to qualitative variations of the stray field, which, however, always decays much faster with a magnetic shell than without it (open black circles). The difference is related to the $\sim 1/r^4$ decay of the stray field for quadrupoles.

V. CONCLUSION

We quantitatively evaluated the advantages of using composite storage cells for perpendicular-shape-anisotropy MTJs, made of a core pillar surrounded by a magnetic shell decoupled from exchange but coupled by dipolar interaction, so that it behaves as a synthetic ferrimagnet with out-of-plane magnetization. The practical realization of such cells could make use of conformal coating techniques, such as atomic layer deposition for the formation of the magnetic shell, around a patterned magnetic tunnel junction. Using both analytical models and micromagnetic simulations, we outline the benefits in terms of enhanced stability and stray-field mitigation in dense arrays. Because of the antiparallel state further promoting perpendicular magnetization besides the shape effect of the individual core, it is possible to consider reducing the core-shell height for a given stability factor, thus reducing the switching voltage necessary to trigger reversal and lowering its switching time.

Making use of an appropriate geometry for stability of around 80 $k_B T$, we compared the use of magnetic shells of Ni versus Co. For both materials, a larger damping allows for a faster reversal, a criterion opposite to the one to follow for classical MTJs. The use of a magnetic shell also greatly reduces the stray field arising from neighboring cells, allowing the technology to be extended to very dense arrays. As an example, we observed a faster reversal for a core-shell element with similar external diameter to that of a single PSA-MTJ. Coupled to a compensated stray field, the proposed geometry offers an increase in the switching speed at accessible voltages. These assets are general to core-shell structures, so they remain valid for other geometries, such as prismatic.

[1] B. Dieny *et al.*, Opportunities and challenges for spintronics in the microelectronic industry, Nat. Electron. **3,** 446 (2020).

[2] H. Sato, S. Ikeda, and H. Ohno, Magnetic tunnel junctions with perpendicular easy axis at junction diameter of less than 20 nm, Jpn. J. Appl. Phys. **56,** 0802A6 (2017).

[3] N. Perrissin, S. Lequeux, N. Strelkov, A. Chavent, L. Vila, L. D. Buda-Prejbeanu, S. Auffret, R. C. Sousa, I. L. Prejbeanu, and B. Dieny, A highly thermally stable sub-20 nm magnetic random-access memory based on perpendicular shape anisotropy, Nanoscale **10,** 12187 (2018).

[4] K. Watanabe, B. Jinnai, S. Fukami, H. Sato, and H. Ohno, Shape anisotropy revisited in single-digit nanometer magnetic tunnel junctions, Nat. Commun. **9,** 663 (2018).

[5] M. Beleggia and M. De Graef, General magnetostatic shape–shape interactions, J. Magn. Magn. Mater. **285,** L1 (2005).

[6] S. Tandon, M. Beleggia, Y. Zhu, and M. De Graef, On the computation of the demagnetization tensor for uniformly magnetized particles of arbitrary shape. Part I: Analytical approach, J. Magn. Magn. Mater. **271,** 9 (2004).

[7] T. P. Almeida, S. Lequeux, A. Palomino, R. C. Sousa, O. Fruchart, I.-L. Prejbeanu, B. Dieny, A. Masseboeuf, and D. Cooper, Quantitative visualization of thermally enhanced perpendicular shape anisotropy STT-MRAM nanopillars, Nano Lett. **22,** 4000 (2022).

[8] S. Lequeux, T. Almeida, N. Caçoilo, A. Palomino, I. L. Prejbeanu, R. C. Sousa, D. Cooper, and B. Dieny, in *2021 IEEE International Memory Workshop (IMW)* (IEEE, Dresden, Germany, 2021), p. 1.

[9] S. Lequeux, N. Perrissin, G. Grégoire, L. Tillie, A. Chavent, N. Strelkov, L. Vila, L. D. Buda-Prejbeanu, S. Auffret, R. C. Sousa, I. L. Prejbeanu, E. D. Russo, E. Gautier, A. P. Conlan, D. Cooper, and B. Dieny, Thermal robustness of magnetic tunnel junctions with perpendicular shape anisotropy, Nanoscale **12,** 6378 (2020).

[10] N. Caçoilo, S. Lequeux, B. Teixeira, B. Dieny, R. Sousa, N. Sobolev, O. Fruchart, I. Prejbeanu, and L. Buda-Prejbeanu, Spin-torque-triggered magnetization reversal in magnetic tunnel junctions with perpendicular shape anisotropy, Phys. Rev. Appl. **16,** 024020 (2021).

[11] B. Jinnai, J. Igarashi, K. Watanabe, T. Funatsu, H. Sato, S. Fukami, and H. Ohno, in *2020 IEEE International Electron Devices Meeting (IEDM)* (IEEE, San Francisco, US, 2020), p. 24.6.1.

[12] B. Jinnai, J. Igarashi, T. Shinoda, K. Watanabe, S. Fukami, and H. Ohno, in *2021 IEEE International Electron Devices Meeting (IEDM)* (IEEE, San Francisco, US, 2021), p. 1.

[13] M. Beleggia, J. Lau, M. Schofield, Y. Zhu, S. Tandon, and M. De Graef, Phase diagram for magnetic nano-rings, J. Magn. Magn. Mater. **301,** 131 (2006).

[14] M. Beleggia, D. Vokoun, and M. De Graef, Demagnetization factors for cylindrical shells and related shapes, J. Magn. Magn. Mater. **321**, 1306 (2009).

[15] H. J. Richter and A. Y. Dobin, Analysis of magnetization processes in composite media grains, J. Appl. Phys. **99**, 08Q905 (2006).

[16] I. Marcos-Alcalde, J. Setoain, J. I. Mendieta-Moreno, J. Mendieta, and P. Gómez-Puertas, MEPSA: Minimum energy pathway analysis for energy landscapes, Bioinformatics **31**, 3853 (2015).

[17] L. D. Buda, I. L. Prejbeanu, U. Ebels, and K. Ounadjela, Micromagnetic simulations of magnetisation in circular cobalt dots, Comput. Mater. Sci. **24**, 181 (2002).

[18] J. C. Slonczewski and J. Z. Sun, Theory of voltage-driven current and torque in magnetic tunnel junctions, J. Magn. Magn. Mater. **310**, 169 (2007).

[19] J. Z. Sun and D. C. Ralph, Magnetoresistance and spin-transfer torque in magnetic tunnel junctions, J. Magn. Magn. Mater. **320**, 1227 (2008).

[20] J. Z. Sun *et al.*, Spin-torque switching efficiency in CoFeB-MgO based tunnel junctions, Phys. Rev. B **88**, 104426 (2013).

[21] T. Taniguchi, An analytical computation of magnetic field generated from a cylinder ferromagnet, J. Magn. Magn. Mater. **452**, 464 (2018).

[22] O. Fruchart, J.-P. Nozières, B. Kevorkian, J.-C. Toussaint, D. Givord, F. Rousseaux, D. Decanini, and F. Carcenac, High coercivity in ultrathin epitaxial micrometer-sized particles with in-plane magnetization: Experiment and numerical simulation, Phys. Rev. B **57**, 2596 (1998).

[23] P. B. Veiga, A. Mora-Hernandez, M. Dammak, S. Auffret, I. Joumard, L. Vila, L. D. Buda-Prejbeanu, I. L. Prejbeanu, B. Dieny, and R. C. Sousa, Control of interface anisotropy for spin transfer torque in perpendicular magnetic tunnel junctions for cryogenic temperature operation, AIP Adv. **13**, 025253 (2023).

[24] L. Wan, T.-W. Wu, N. Smith, T. Santos, G. Mihajlovic, J.-L. Li, K. Patel, N. D. Melendez, B. Terris, and J. A. Katine, Fabrication and individual addressing of STT-MRAM bit array with 50 nm full pitch, IEEE Trans. Magn. **58**, 1 (2022).

[25] L. Wu, S. Rao, M. Taouil, E. J. Marinissen, G. Sankar Kar, and S. Hamdioui, in *2020 Design, Automation & Test in Europe Conference & Exhibition (DATE)* (IEEE, Grenoble, France, 2020), p. 1211.

[26] A. V. Khvalkovskiy, D. Apalkov, S. Watts, R. Chepulskii, R. S. Beach, A. Ong, X. Tang, A. Driskill-Smith, W. H. Butler, P. B. Visscher, D. Lottis, E. Chen, V. Nikitin, and M. Krounbi, Basic principles of STT-MRAM cell operation in memory arrays, J. Phys. D: Appl. Phys. **46**, 074001 (2013).